Arabian Journal of Chemistry (2022) **15**, 103580

King Saud University

Arabian Journal of Chemistry

www.ksu.edu.sa
www.sciencedirect.com

ORIGINAL ARTICLE

Controllable synthesis of hierarchical nanoporous carbon@Ni(OH)$_2$ rambutan-like composite microspheres for high-performance hybrid supercapacitor

Na Li [a], Kai Yuan [a], Tengjia Gao [a], Shun Li [b], Jianliang Qin [c], Yirong Zhu [a], Jingjing Du [b], Lijian Xu [b,*], Jianxiong Xu [b,c]

[a] *Hunan Key Laboratory of Electrochemical Green Metallurgy Technology, College of Materials and Advanced Manufacturing, Hunan University of Technology, Zhuzhou 412007, PR China*
[b] *Hunan Key Laboratory of Biomedical Nanomaterials and Devices, College of Life Sciences and Chemistry, Hunan University of Technology, Zhuzhou 412007, PR China*
[c] *Guangxi Danquan Wine Co., Ltd, Minxing North Road, Chengguan Town, Nandan county, Hechi 530000, PR China*

Received 15 September 2021; accepted 16 November 2021
Available online 22 November 2021

KEYWORDS

Nickel hydroxide;
Hierarchical nanoporous carbon;
Hybrid supercapacitors;
Electrochemical performance

Abstract Design of electrode materials with excellent electrochemical properties for advanced energy storage device are important to the sustainable development of energy resources. In this manuscript, a novel hierarchical nanoporous carbon@nickel hydroxide (HNCMs@Ni(OH)$_2$) composites were prepared through simple in-situ chemical deposition of Ni(OH)$_2$ nanocrystals on HNCMs. By tailoring the deposition amount, core–shell structured rambutan-like HNCMs@Ni(OH)$_2$ microspheres with hairy nickel hydroxide nanocrystal covered on HNCMs were obtained. Ascribed to the high specific capacitance of nickel hydroxide and the interconnected hierarchical porous structure of HNCMs, the resultant rambutan-like HNCMs@Ni(OH)$_2$ microspheres as electrode materials display outstanding electrochemical properties including high specific capacity of 248.9 mAh/g at 1 A/g and good capacitance retention of 62.9% at 20 A/g. Furthermore, a hybrid supercapacitor with rambutan-like HNCMs@Ni(OH)$_2$ microspheres as cathode and HNCMs as anode were assembled and showed a comparable energy density of 41.3 Wh/kg at the power density of 173.3 W/kg and high capacity retention of 85.2% after 20,000 cycles at 5 A/g. As a proof of concept example, the fabricated hybrid supercapacitor can be utilized as energy source to instantaneous light up a red LED indicator. We envisioned that the as-prepared rambutan-like HNCMs@Ni

* Corresponding author.
E-mail address: xlj235@hut.edu.cn (L. Xu).
Peer review under responsibility of King Saud University.

Production and hosting by Elsevier

https://doi.org/10.1016/j.arabjc.2021.103580

$(OH)_2$ microspheres have great potential in constructing of advanced energy storage devices.

1. Introduction

As an electrochemical energy storage device, supercapacitors in the past decades have obtained increasing attention because of their brilliant performances such as excellent cycle stability, fast charging-discharging capability, high power density, *etc* (Simon et al., 2014; Choi et al., 2020; Tang et al., 2021; Zeng et al., 2019; Lokhande et al., 2020a; Zhang et al., 2019). However, the low energy density still hindered their practical applications, especially in peak power assistance and emergency power supply for electric vehicles (Raza et al., 2018; Yan et al. 2014; Zhou et al., 2019; Du et al., 2020). Therefore, significant interests have been paid on the construction of supercapacitors with large power (P) and energy density (E). Based on the equation of $E = 0.5CV^2$, extending the operating potentials (V) window and increasing the specific capacitance (C) are vital to obtain supercapacitors with a high value of E (Che et al., 2020; Yang et al., 2019). Recently, fabrication of hybrid supercapacitors has been considered an effective approach to raise the E value of supercapacitors without compromising the power density (Muzaffar et al., 2019; Chodankar et al., 2020). Usually, a hybrid supercapacitor is composed of a battery-type active material as the anode to obtain a larger capacitance and a capacitor-type material as the cathode to improve the voltage window, therefore resulting in supercapacitors with high energy density (Afif et al., 2019; Liu et al., 2020; Jiang et al., 2020). Previous studies have shown that rational design of battery-type active material is crucial for preparation of hybrid supercapacitor with enhanced electrochemical performance, such as long-life energy storage, high-rate performance, high value of energy density and power density (Liang et al., 2021).

Recently, a variety of materials (including transition metal hydroxides, metal oxides, and conductive polymer) have been extensively researched as cathodes because of their high theoretical C value (Gonçalves et al., 2020; Nguyen et al., 2019; Hong et al., 2021; Ou et al., 2019; Lu et al., 2021a; Yao et al., 2019). Particularly, nickel hydroxide with a layered structure possesses high theoretical C value of 289.2 mAh/g and is considered to be an attractive candidate (Brisse et al., 2018). Nevertheless, bulk nickel hydroxide generally displays low C value, inferior rate performance, and poor durability due to the low level of materials utilization ratio, poor electronic conductivity, irreversible phase transition as well as large volume variation during the cycling process (Liu et al., 2018; Zhang et al., 2018). Pioneers have tried to synthesize nanosized nickel hydroxide such as nanospheres (Guo et al., 2021), nanotubes (Zhou et al., 2020a), nanosheets (Li et al., 2020), and nanoflowers (Hong et al., 2021), which offer large specific surface area and more electroactive sites to enhance the rate capability and the specific capacity. However, because of the self-agglomeration among nano-sized nickel hydroxide during the repeated redox reaction in the charging/discharge process, the property of pure $Ni(OH)_2$ applied in electrodes is always unsatisfactory (Yang et al., 2019; Wang et al., 2019). An alternative way is to fabricate a composite combined nickel hydroxide with conductive carbon. To date, various $Ni(OH)_2$/carbon materials have been prepared by in-situ deposition of nickel hydroxide crystals on carbon materials including carbon nanotubes (Abitkar et al., 2019), carbon aerogels (Wang et al., 2018), porous carbon materials (Chen et al., 2020), graphene (Mohammed et al., 2020), etc. The carbonaceous materials not only enhance the electrical conductivity of the composite materials but also act as a scaffold to govern the growth of nickel hydroxide and suppress the agglomeration of the nickel hydroxide, resulting in composite materials with superior electrochemical performance. Comparatively speaking, porous carbon materials are more suitable as the scaffold for their high specific surface area and interconnected porous structure (Xu et al., 2018; Wang et al., 2020; Luo et al., 2021). For instance, Zhang et al. reported the porous polyimide-derived carbon aerogel as a conductive scaffold for nickel hydroxide nanosheets, and the prepared hybrids displayed a C value of 149.2 mAh/g at 1 A/g (Zhang et al., 2018). Choi et al. fabricated carbon/$Ni(OH)_2$ with mesoporous structure and it possessed a C value of 223 mAh/g at 5 mV/s (Choi et al., 2017). Fu et al. successfully prepared a hollow mesoporous carbon sphere enwrapped nickel hydroxide nanosheets showing a C value of 213.2 mAh/g at 1 A/g (Fu et al., 2018). However, a non-negligible problem is the growth of nickel hydroxide nanocrystals on porous carbon inevitably led to a serious blockage of the pores and suppressed the electrochemical performance of the composite.

In this work, core–shell structured rambutan-like HNCMs@Ni$(OH)_2$ microspheres were elaborately designed and prepared by in-situ deposition of nickel hydroxide crystals on HNCMs for construction of high-performance hybrid supercapacitor. The general idea of this work was schematically shown in Scheme 1. Initially, the HNCMs were synthesized by dynamic dual template strategy as reported in our recent works (Xu et al., 2020; Xie et al., 2020), which possessed large specific surface area and interconnected multimodal porous structure (micropores-mesopores-interstitial pores). A series of HNCMs@Ni$(OH)_2$ composite materials were controllably synthesized by tailoring the deposition amount of nickel hydroxide nanocrystals. Moreover, the relationship between the structure and electrochemical performance of HNCMs@Ni$(OH)_2$ was revealed. Core-shell structured rambutan-like HNCMs@Ni$(OH)_2$ microspheres with optimized electrochemical properties including a high value of C and superior rate performance can be prepared in consideration for the balance between adequate nickel hydroxide nanocrystals and the maintenance of the hierarchical nanoporous structure of HNCMs. In addition, a hybrid supercapacitor was assembled employing the optimized rambutan-like HNCMs@Ni$(OH)_2$ microspheres as cathode and HNCMs as anode and its electrochemical performances were evaluated.

2. Experimental

2.1. Materials

All chemical reagents were of analytical grade and used without further treatment. Hexadecylpyridinium chloride (CPC), ammonia ($NH_3{\cdot}H_2O$, 25%-28%), hydrofluoric acid (HF, ≥40%), nickel sulfate hexahydrate ($NiSO_4{\cdot}6H_2O$), and potassium persulfate ($K_2S_2O_8$) were purchased from Aladdin Industrial Cooperation. Poly (acrylic acid) (PAA) (25 wt% solutions in water) was received from Acros organics. Tetraethylsiloxane (TEOS) and sucrose were obtained from Alfa Aesar.

2.2. Synthesis of hierarchically nanoporous carbon materials (HNCMs)

In a typical synthesis, 0.54 g CPC and 4.0 g PAA were firstly dissolved in 30 mL deionized water under rapid stirring to obtain a homogeneous solution. Then, 2.0 g ammonia was slowly added to the above solution, and a milky white suspension was obtained after vigorous stirring for 30 min. Later on, TEOS (2.1 g, 10 mmol) and sucrose (5.0 g, 150 mmol) were added to the above suspension, the mixture was stirred for 30 min and transferred into Teflon-lined stainless steel auto-

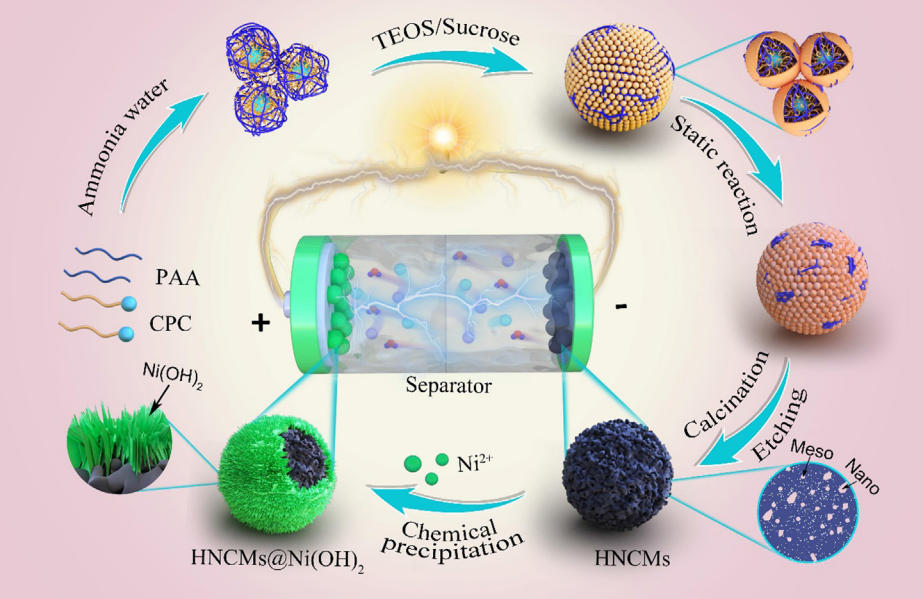

Scheme 1 Schematic illustrating the fabrication of HNCMs@$Ni(OH)_2$ composites and assembly of HNCMs@$Ni(OH)_2$//HNCMs hybrid supercapacitor.

clave maintained at 80 ℃ for 48 h. After cooling the room temperature, the solid product was washed several times with deionized water and ethanol by centrifugation and dried at 50 ℃ overnight. The silica/carbon composite was obtained after annealing at 800 ℃ for 3 h in Ar flow at a heating rate of 5 ℃/min. Finally, the silica was etched by hydrofluoric acid (HF, 10 wt%), washed with deionized water to neutrality, and freeze-dried to obtain hierarchical nanoporous carbon materials (HNCMs).

2.3. Synthesis of hierarchical nanoporous carbon materials@nickel hydroxide nanosheets (HNCMs@$Ni(OH)_2$) core–shell composites

Typically, a certain amount (0.21 g ~ 2.5 g) of $NiSO_4{\cdot}6H_2O$ (the concentration of Ni^{2+} in the solution at 0.02 ~ 0.24 M) and $K_2S_2O_8$ (6.80 mg ~ 81.0 mg with concentration ranging from 0.62 to 7.5 mM) were dissolved in 40 mL deionized water with vigorous stirring to obtain a uniform solution. The molar ratio of $NiSO_4{\cdot}6H_2O$: $K_2S_2O_8$ was kept at 32: 1. Then 100 mg HNCMs was uniformly dispersed into the mixed solution by ultrasound. After stirring for 2 h, 0.3 mL ammonia was slowly added dropwise to the mixed solution and stirred for 30 min. The HNCMs@$Ni(OH)_2$ composite was obtained by centrifugation, washed by deionized water and ethanol, and finally vacuum dried. A series of HNCMs@$Ni(OH)_2$ composites were prepared with the concentration of Ni^{2+} in the solution at 0.02, 0.04, 0.08, 0.12, 0.20, and 0.24 M, while other experimental conditions were unchanged. For comparison, pure $Ni(OH)_2$ sample was prepared with the concentration of Ni^{2+} in the solution at 0.12 M without adding of HNCMs. All the experimental parameters were summarized in **Table S1**.

2.4. Material characterizations

The morphology and structure of the as-made samples were examined by Field-emission scanning electron microscopy (FE-SEM), transmission electron microscopy (TEM), high-resolution TEM (HR-TEM) images, and EDX mapping were collected on Thermal scientific Apreo S LoVac instrument and JEOL JEM 2100F microscope at an acceleration voltage of 200 kV. X-ray powder diffraction (XRD) patterns were performed on a Rigaku Model D/max-2500 diffractometer, with Cu Kα (λ = 0.15406 nm) radiation and the scanning angles (2θ) ranging from 5° to 90°. The N_2 adsorption measurement was performed on the Micromeritics TriStar II 3020 sorption analyzer. Fourier transform infrared (FT-IR) spectra were obtained using a Bruker VECTOR 22 spectrometer. X-ray photoelectron spectra (XPS) was measured on Thermo Kalpha with radiation of Mono Al *K*α.

2.5. Electrochemical characterization

The electrochemical properties of the individual electrode were evaluated using a CHI 760E electrochemical workstation (Shanghai Chenhua Instrument Co., China) in a three-electrode system with a 2 M KOH aqueous electrolyte, in which Hg/HgO electrode and Pt foil were used as the reference electrode and counter electrode, respectively. The working electrode was prepared by mixing the active materials, acetylene black and polytetrafluoroethylene (PTFE, 60 wt%) with ethanol in a mass ratio of 7:2:1. The slurry was filled into the nickel foam substrate using a spatula and dried at 80℃ overnight, then pressed at 10 MPa for 3 s to ensure good electrical contact between the foamed nickel substrate and the active material. The mass loading of the active materials was about 1.0 mg/cm^2. The cyclic voltammetry (CV) and galvanostatic charge–discharge (GCD) measurements were tested within 0 V ~ 0.6 V and 0 ~ 0.5 V at different scan rates, respectively. The electrochemical impedance spectroscopy (EIS) was performed at the range from 0.01 ~ 100 kHz under the open circuit potential at an amplitude of 5 mV.

The specific capacity of a single electrode is calculated by the following Eq. (1) (Chavan et al., 2021):

$$C = \frac{I\Delta t}{3.6m} \quad (1)$$

Where C (mAh/g) is the specific capacity of electrode, I (A) is discharge current, Δt (s) is the discharge time, m is the mass of the active material (g) and ΔV (V) is the working potential window.

2.6. Fabrication of HNCMs@Ni(OH)$_2$//HNCMs hybrid supercapacitor device

The hybrid supercapacitor device was fabricated with HNCMs@Ni(OH)$_2$ as the cathode electrode, HNCMs as the anode electrode, polypropylene membrane as separator, and 2 M KOH as the electrolyte. The negative electrode was prepared by mixing HNCMs, acetylene black, and polytetrafluoroethylene (PTFE) in a mass ratio of 8:1:1. To better balance the charge of the positive and negative electrodes in the hybrid capacitor device, the mass ratio of the two electrodes is calculated by the following Eq. (2):

$$\frac{m_+}{m_-} = \frac{C_-\Delta V_-}{C_+\Delta V_+} \quad (2)$$

where m_+ (g) and m_- (g) are the masses of the positive electrode and negative electrode, C_+ (mAh/g) and C_- (mAh/g) are specific capacity of positive and negative, respectively. ΔV_+ (V) and ΔV_- (V) are potential ranges of positive electrode and negative electrode, respectively. The optimized charge balance mass ratio between HNCMs@Ni(OH)$_2$ (1.0 mg) and HNCMs (3.3 mg) electrodes was found to be 0.3.

The specific capacitance of the device was calculated by the following equation:

$$C_H = \frac{I\Delta t}{M\Delta V} \quad (3)$$

where C_H (F/g) is the specific capacitance of the hybrid supercapacitor, I (A) is the discharge current, Δt (s) is the discharge time, M (g) is the total mass of effective active materials of positive and negative electrodes ($M = m_+ + m_-$). ΔV (V) is the potential range.

The energy density (E, Wh/kg) and power density (P, W/kg) of the hybrid supercapacitor were calculated based on the total mass of the effective active material by the following equation, respectively:

$$E = \frac{C_H\Delta V^2}{2 \times 3.6} \quad (4)$$

$$P = \frac{E \times 3600}{\Delta t} \quad (5)$$

3. Results and discussion

3.1. Controlled fabrication of HNCMs@Ni(OH)$_2$

Firstly, the HNCMs@Ni(OH)$_2$–6 sample was prepared by in-situ growth of Ni(OH)$_2$ crystals on HNCMs with the concentration of Ni^{2+} at 0.12 M. The chemical component, crystal structure, and morphology of the synthesized HNCMs@Ni(OH)$_2$–6, as well as HNCMs and Ni(OH)$_2$, were comparatively studied by FTIR, XRD, FE-SEM, and TEM, respectively. Fig. 1**a** shows the FTIR spectra of the three samples. As for the HNCMs, two typical peaks at approximately 3444 and 1631 cm^{-1} belonged to the –OH tensile vibration from inserted water and the bending vibration of water molecules, respectively, were observed (Lokhande et al., 2019). Another two weak absorption peaks located at 1719 and 1087 cm^{-1} were assigned to the stretching vibration of C = O (carbonyl) and antisymmetric stretching vibration of the C-O bond, respectively (Xu et al., 2020; Zhou et al., 2020b). With regard to nickel hydroxide, except for the obvious peaks of adsorbed water, the characteristic peak at 678 cm^{-1} and was 463 cm^{-1} were originated from the bending vibration of the Ni-O-H bond, and the stretching vibration of the Ni-O bond (Shakir et al., 2020). Moreover, two peaks at 1120 and 932 cm^{-1} were related to the SO_4^{2-} anion, which was derived from the reduction of $S_2O_8^{2-}$ (Zhang et al., 2020). The FTIR spectrum of HNCMs@Ni(OH)$_2$–6 was similar to that of pure Ni(OH)$_2$, but the peak intensity decreased somewhat, potentially suggesting the presence of Ni(OH)$_2$ in HNCMs. Fig. 1**b** demonstrated the XRD patterns of three samples. For the XRD pattern of HNCMs (red curve), two characteristic peaks located at 24.2° and 43.4° were attributed to the facet (002) and facet (100) of graphite, respectively, which indicated the existence of a certain graphite layer in HNCMs (Ping et al., 2019a; Han et al., 2019). The XRD pattern of pure Ni(OH)$_2$ (blue curve) was well-matched with standard card (JCPDS: 22–0444) of α-Ni(OH)$_2$, where the several feature peaks at 11.5, 23.7, 33.5, and 59.5 were corresponding to the crystal planes of (001), (002), (110), and (300), respectively (Fu et al.,2018; Zhang et al., 2020). Both the typical diffraction peaks belong to the α-Ni(OH)$_2$ and graphited HNCMs could be found in the XRD pattern of HNCMs@Ni(OH)$_2$–6. Moreover, the intensity of all peaks significantly decreases due to the formation of small size nickel hydroxide crystals on HNCMs@Ni(OH)$_2$.

To get an intuitive observation about the formation of HNCMs@Ni(OH)$_2$, the FE-SEM was applied to track the morphology change before and after deposition of Ni(OH)$_2$ on HNCMs. In **Fig. S1(a, b)**, the fabricated HNCMs is walnut-like microspheres with diameter ranging from 400 to 900 nm. Differently, the prepared Ni(OH)$_2$ particles exhibit a micro-flowers structure assembled by the agglomeration of nickel hydroxide nanosheets (**Fig. S1(c, d)**). Interestingly, HNCMs@Ni(OH)$_2$–6 inherited the spherical morphology of HNCMs (Fig. 1**c**), and presented a larger size, suggesting the presence of Ni(OH)$_2$ nanocrystals on HNCMs. The resultant HNCMs@Ni(OH)$_2$–6 was more likely as hairy microspheres (Fig. 1**d**). We called this structure as "rambutan-like" microspheres. No obvious Ni(OH)$_2$ crystal aggregates were observed implying that the deposition of Ni(OH)$_2$ nanocrystals strictly occurred on HNCMs scaffold. The reason could be explained as follows. During this growing process, the Ni^{2+} in the solution was adsorbed on the HNCMs negative charge surface of HNCMs via electrostatic interaction. Meanwhile, the presence of potassium persulfate promoted the ionization of ammonia water ensuring sufficient OH^- to react with Ni^{2+} to produce Ni(OH)$_2$, which could be acted as a seed and anchored on the surface of HNCMs, then gradually grew into "hairy" Ni(OH)$_2$ nanocrystals.

The nitrogen adsorption–desorption curves of the three samples were shown in Fig. 1**e**. As shown, all of them exhibit a typical Ⅳ type isotherm along with a distinct hysteresis loop, implying the mesoporous structure of the samples. The calcu-

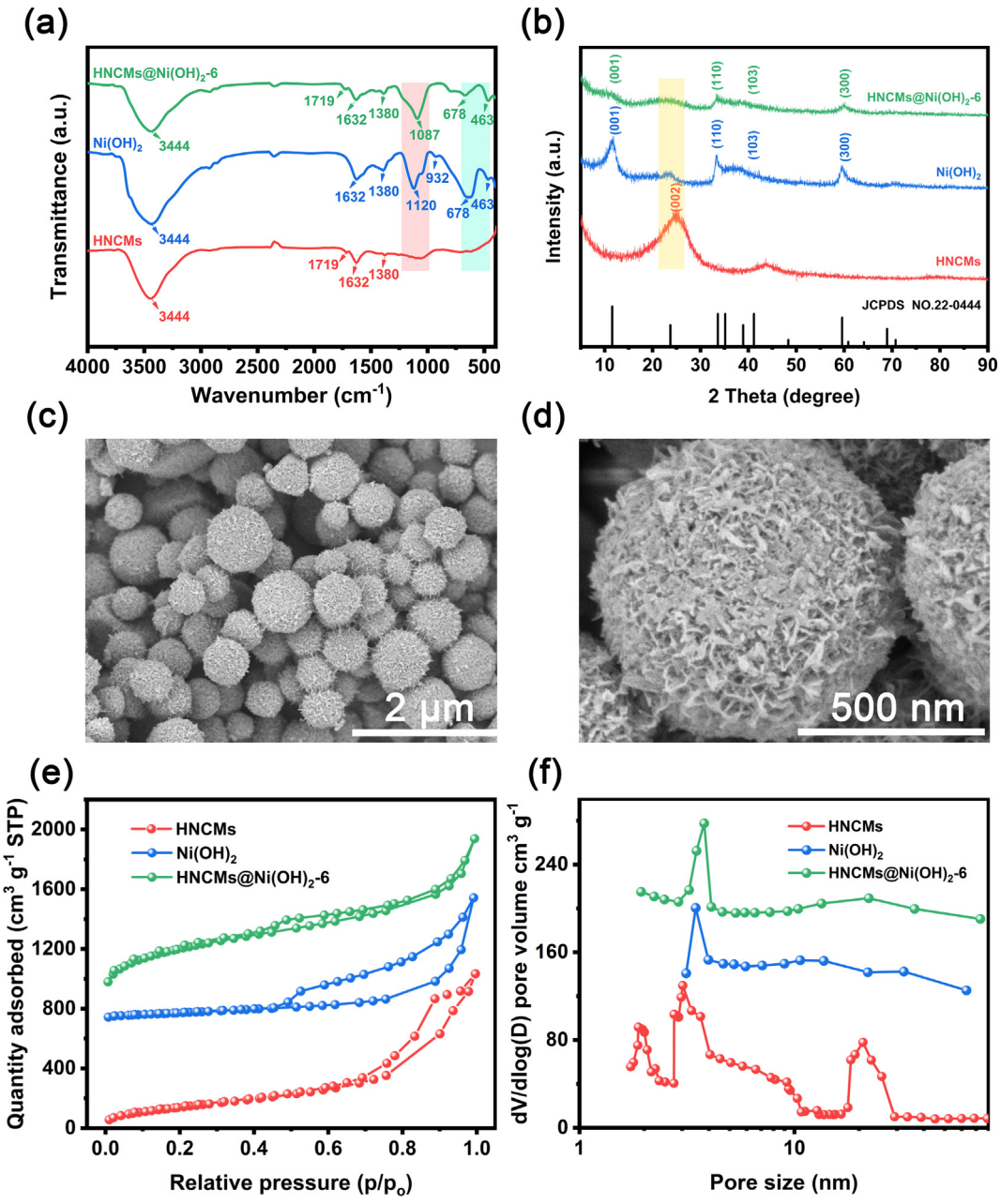

Fig. 1 Characterization of HNCMs, Ni(OH)$_2$, and HNCMs@Ni(OH)$_2$. (a) FTIR spectra, (b) XRD patterns, (c, d) FE-SEM images of HNCMs@Ni(OH)$_2$–6, (e) adsorption/desorption isotherms of nitrogen, and (f) the pore size distribution curves.

lated specific surface area of HNCMs@Ni(OH)$_2$–6 was 286.6 m^2/g, which was smaller than HNCMs (735.3 m^2/g). The reduction of the specific surface area may be due to that the deposition of Ni(OH)$_2$ inevitably blocked the mesopore of the HNCMs to some extent. Compared with nickel hydroxide micro-flower (59.8 m^2/g), HNCMs@Ni(OH)$_2$–6 owned a larger specific surface area of 286.6 m^2/g, potentially suggesting that the HNCMs@Ni(OH)$_2$–6 retained the porous structure of HNCMs. Moreover, the pore size distribution curve of HNCMs@Ni(OH)$_2$–6 (Fig. 1**f**) presented a sharp mesopore peak centered at 3.9 nm and a wide nanopores peak at a range of 13.4 nm to 28.0 nm, similar to that of the HNCMs. The results further demonstrated that the HNCMs@Ni(OH)$_2$–6 still had a hierarchical nanoporous structure in the inner core.

Furthermore, the interior structure of the as-prepared HNCMs and HNCMs@Ni(OH)$_2$–6 were compared by TEM observation. As shown in Fig. 2**a**, the hierarchically nanoporous internal structure of HNCMs could be observed, where mesoporous and secondary interstitial nanoporous were visible. Fig. 2**b and c** revealed that the HNCMs@Ni(OH)$_2$–6 still maintained the hierarchically nanoporous structure. Besides, hairy nickel hydroxides were wrapped on the surface of HNCMs to form the core–shell structured rambutan-like HNCMs@Ni(OH)$_2$–6 microspheres. Undoubtedly, the hierarchically nanoporous internal structure of HNCMs@Ni(OH)$_2$–6 was beneficial for the transportation of ions in materials. The high-resolution TEM (HRTEM) image and selected area electron diffraction (SAED) pattern of the HNCMs@Ni(OH)$_2$–6

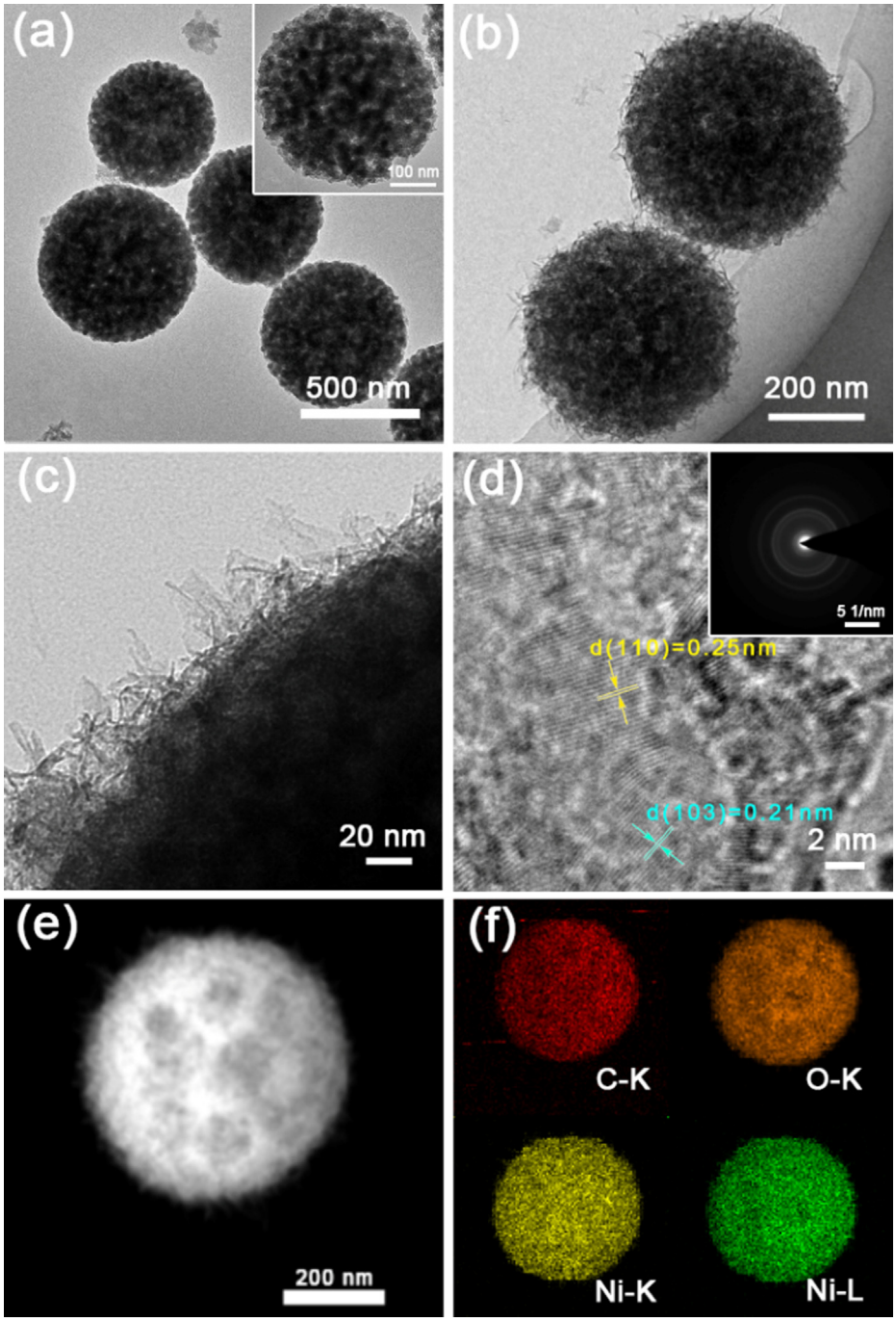

Fig. 2 (a) TEM images of HNCMs, (b, c) TEM images of HNCMs@$Ni(OH)_2$–6, (d) HRTEM image of hairy crystal (inset is the corresponding SAED pattern), (e, f) EDS mapping images of HNCMs@$Ni(OH)_2$–6.

were displayed in Fig. 2**d** and the corresponding inset. The interlayer *d*-spacing values of the hairy crystals were about 0.25 and 0.22 nm matched with the facets (1 1 0) and (1 0 3) of α-$Ni(OH)_2$ respectively. The SAED pattern showed multiple sharp diffraction rings, demonstrating the polycrystalline characteristics of the hairy nickel hydroxide in HNCMs@$Ni(OH)_2$–6. In Fig. 2**e and** Fig. 2**f**, EDS mapping images showed that the elements including carbon, oxygen, and nickel elements were homogeneously dispersed in the rambutan-like HNCMs@$Ni(OH)_2$–6 microspheres, indicating the uniform distribution of nickel hydroxide in HNCMs.

The elemental valence states of HNCMs@$Ni(OH)_2$–6 were also characterized using XPS. Elements of Ni, O, and C were detected in the survey XPS spectrum (Fig. 3**a)**. As shown in Ni 2p spectrum (Fig. 3**b)**, the two major peaks at 856.4 and 874.0 eV corresponded to the Ni $2p_{3/2}$ and Ni $2p_{1/2}$ spin–orbit peaks, respectively (Jing et al., 2021). Besides, a couple of satellite peaks centered at 862.1 and 880.3 eV with the energy

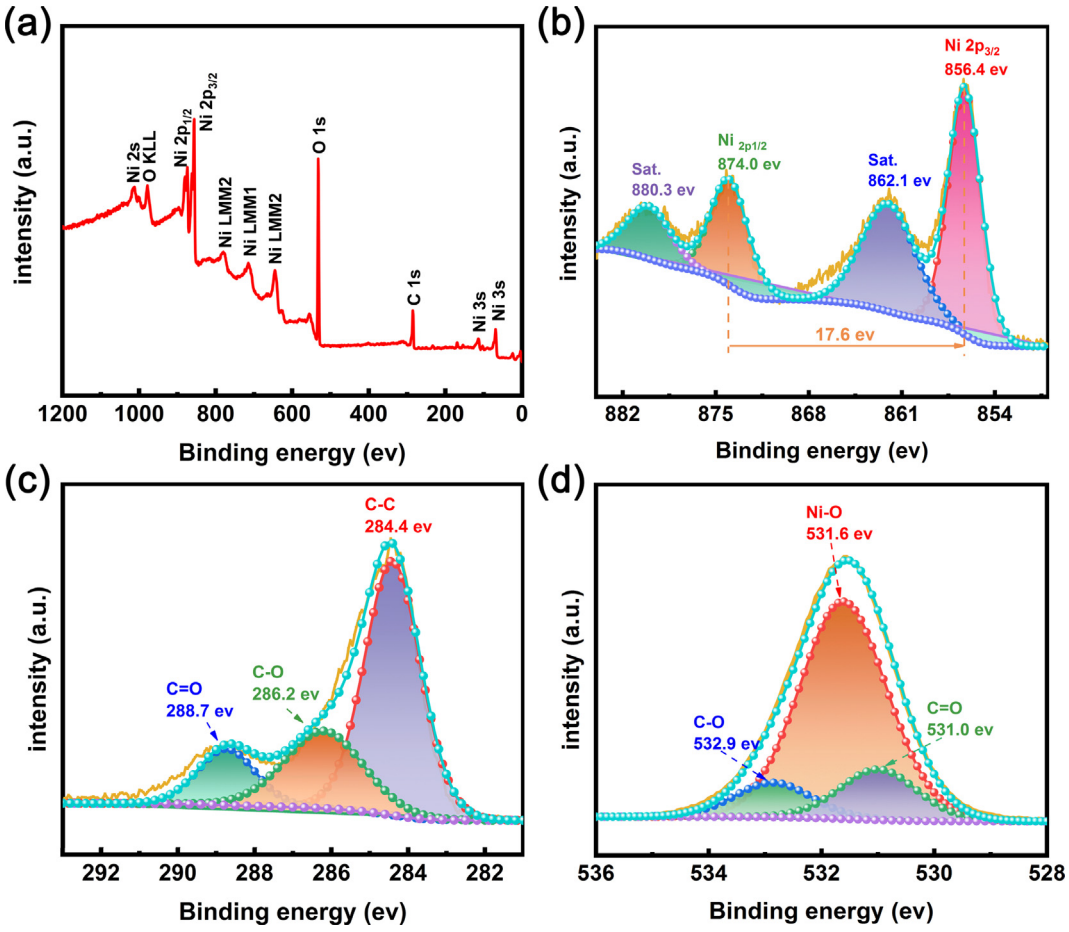

Fig. 3 XPS spectrum of HNCMs@Ni(OH)$_2$–6, (a) survey XPS spectrum, (b) Ni 2p, (c) C 1 s, and (d) O 1 s.

difference of 18.2 eV were also observed, indicative of the bivalent nickel (Ji et al., 2021; Feng et al., 2020). In the C 1 s spectrum (Fig. 3**c**), the major peak at 284.4 eV demonstrated the existence of graphitic or graphite-like sp^2 C-C bonds, while two weak peaks located at 286.2 and 288.7 eV were attributed to C-O and C = O bonds (Liu et al., 2019; Du et al., 2021). The C element was mainly originated from HNCMs. The existence of oxygen-containing groups in HNCMs not only facilitated the deposition of nickel hydroxide but also increase the wettability of the electrode–electrolyte interface. In addition, the O 1 s spectra (Fig. 3**d**) revealed that there were three peaks with binding energy at 531.0, 531.6, and 532.9 eV, which belonged to C = O, Ni-O, and C-O bonds, respectively, further confirming the presence of nickel hydroxide in the synthesized HNCMs@Ni(OH)$_2$–6 (Mohammed et al., 2020; Han et al., 2020).

It is well known that the concentration of Ni^{2+} in the solution has great impacts on the deposition of Ni(OH)$_2$ on HNCMs and therefore influences the structure of the resultant HNCMs@Ni(OH)$_2$. Given this, a series of HNCMs@Ni(OH)$_2$ composites were prepared with the concentration of Ni^{2+} in the solution at 0.02, 0.04, 0.08, 0.12, 0.20 and 0.24 M. The as-synthesized products were marked as HNCMs@Ni(OH)$_2$-X (X = 1, 2, 4, 6, 10 and 12), respectively. The morphology of the HNCMs@Ni(OH)$_2$-X was systematically observed by FE-SEM and TEM. Fig. 4**a1-d1** demonstrated that the resultant HNCMs@Ni(OH)$_2$ composites presented as uniform core–shell structured rambutan-like HNCMs@Ni(OH)$_2$ microspheres as Ni^{2+} in the system was kept below 0.12 M of concentration. Generally, the amount of nickel hydroxide on HNCMs increased and the porosity decreased with the increase of the Ni^{2+} concentration (Fig. 4-**a2-d2 and a3-d3**). When the concentration of Ni^{2+} in the system at 0.2 and 0.24 M, besides the HNCMs@Ni(OH)$_2$ microspheres, obvious nickel hydroxide aggregates were found on HNCMs@Ni(OH)$_2$, as shown in Fig. 4**e1-f1**. This might be due to the solution phase nucleation of the excessive Ni^{2+}. Moreover, the resultant HNCMs@Ni(OH)$_2$ microspheres exhibited flower-like microspheres with nickel hydroxide nanosheet on the surface (Fig. 4**e2-f2**) and had no obvious porous inner structure as shown in the TEM images (Fig. 4**e3-f3**). The porosity of the HNCMs@Ni(OH)$_2$ composite microspheres were further characterized by N_2 adsorption measurement. The N_2 adsorption/desorption isothermal curves were shown in **Fig. S2** and the pore structural parameters were summarized in **Table S2**. As manifested in **Fig. S2** and **Table S2**, the HNCMs@Ni(OH)$_2$–6 exhibited the highest specific surface area (286.6 m^2/g) and the largest pore volume (0.28 cm^3/g).

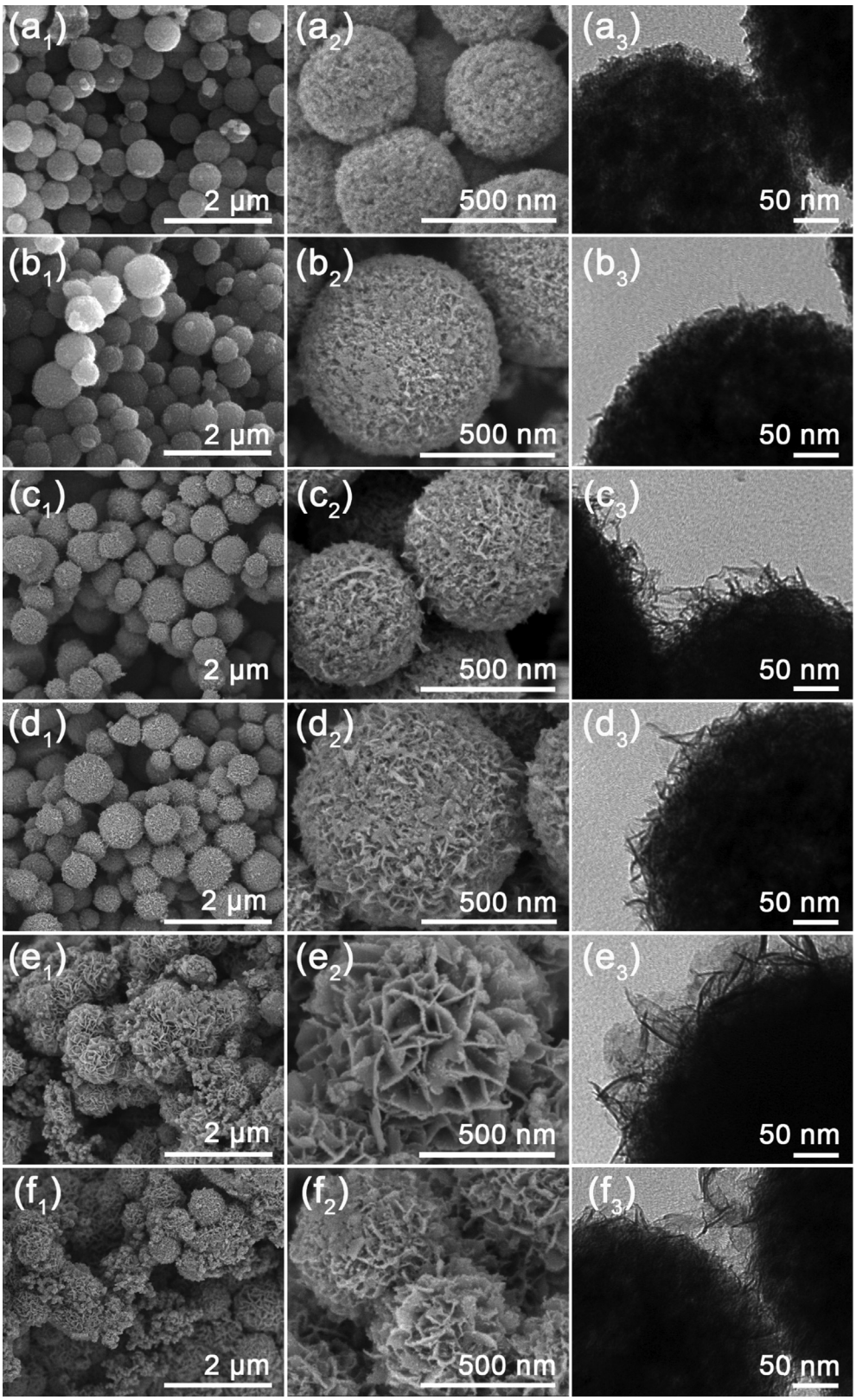

Fig. 4 TEM and FE-SEM images of (a_1-a_3) HNCMs@$Ni(OH)_2$–1, (b_1-b_3) HNCMs@$Ni(OH)_2$–2, (c_1-c_3) HNCMs@$Ni(OH)_2$–4, (d_1-d_3) HNCMs@$Ni(OH)_2$–6, (e_1-e_3) HNCMs@$Ni(OH)_2$–10, and (f_1-f_3) HNCMs@$Ni(OH)_2$–12.

3.2. Comparative study on the electrochemical properties of the HNCMs@Ni(OH)$_2$ composites electrodes

Generally, adequate nickel hydroxide and the maintenance of hierarchical nanoporous of HNCMs has been considered to be important for HNCMs@Ni(OH)$_2$ composites having excellent electrochemical properties. Subsequently, the electrochemical behaviors of various HNCMs@Ni(OH)$_2$ composites were compared. Fig. 5**a** compares the cyclic voltammetry (CV) curves of various HNCMs@Ni(OH)$_2$ electrodes scanned at 5 mV/s in the potential window of 0 to 0.6 V. A couple of faradaic redox peaks were presented for each electrode, which originated from the reversible redox reaction between Ni^{2+} and Ni^{3+}, implying a typical characteristic of battery behavior (Zhang et al., 2018; Lokhande et al., 2020b). Moreover, the CV curve of the HNCMs@Ni(OH)$_2$–6 electrode exhibited the largest peak current and integral area, suggesting the highest value of *C* (Upadhyay et al., 2019). In addition, all galvanostatic charge–discharge (GCD) curves (Fig. 5**b)** presented apparent potential platforms corresponding to the faraday redox reaction (Fu et al., 2018; Lokhande et al., 2018). According to **Eq. (1)**, the *C* value of nickel hydroxide and HNCMs@Ni(OH)$_2$-X (X = 1, 2, 4, 6, 10, and 12) were calculated to be 125.7, 146.2, 156.7, 219.5, 248.9, 190.9, and 168.9

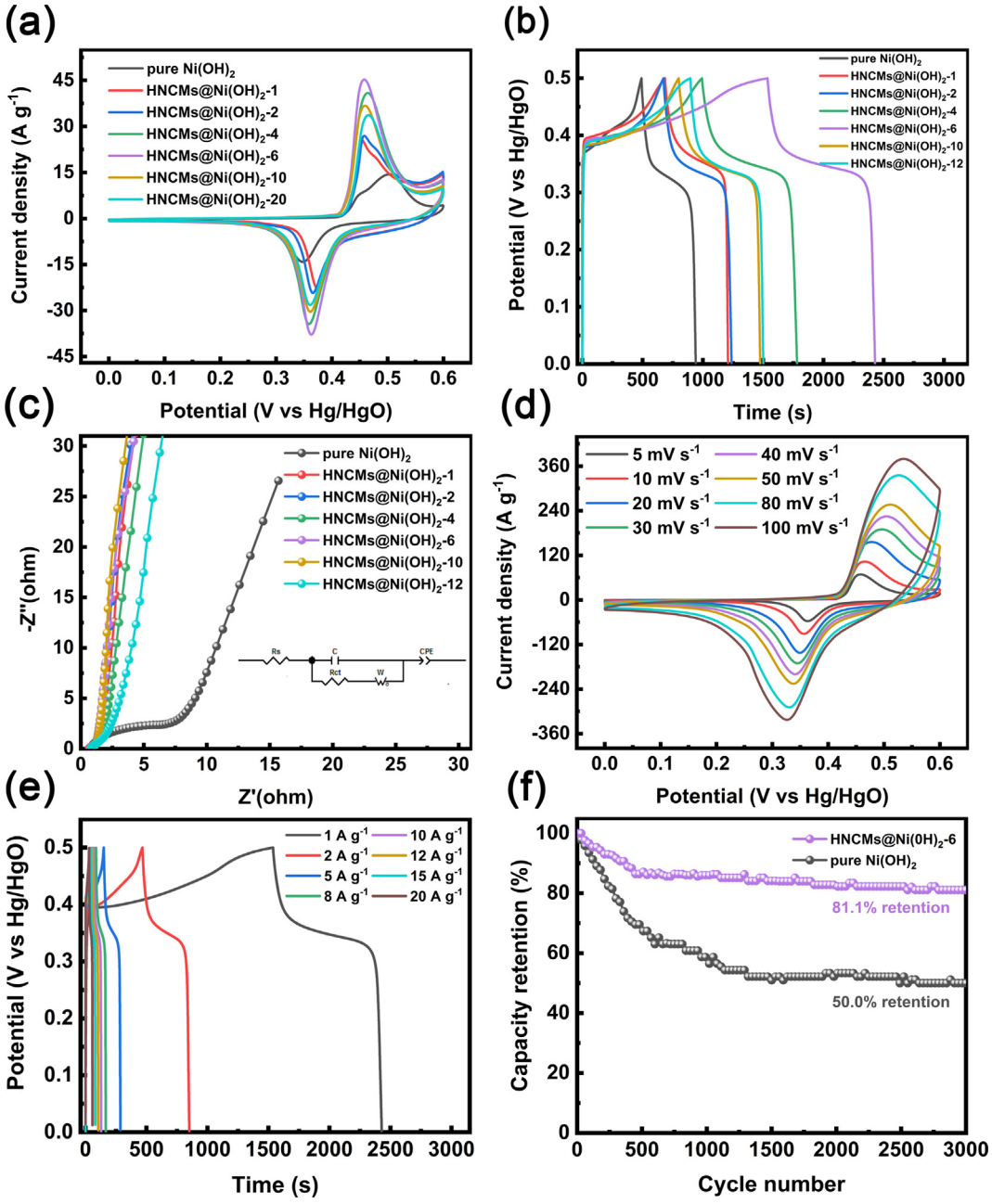

Fig. 5 The electrochemical performance of HNCMs@Ni(OH)$_2$-X including (a) CV curves scanned at 5 mV/s, (b) GCD curves obtained at 1 A/g, and (c) EIS files. The electrochemical properties of HNCMs@Ni(OH)$_2$–6 including (d) CV curves *vs* scan rate, (e) GCD curves *vs* current density, and (f) cycle performance.

mAh/g, respectively. Compared with nickel hydroxide, all the HNCMs@Ni(OH)$_2$-X showed a higher *C* value due to the enhanced conductivity of HNCMs. Besides, the value of *C* from HNCMs@Ni(OH)$_2$–1 to HNCMs@Ni(OH)$_2$–6 gradually increased in turn because of the increased amount of nickel hydroxide in the composites. However, HNCMs@Ni(OH)$_2$–10 and HNCMs@Ni(OH)$_2$–12 with a larger amount of nickel hydroxide owned a reduced *C* value. It might be due to the agglomeration of nickel hydroxide crystals on HNCMs and seriously blocked the pore channels and hindered the ion transportation in the composite materials. Overall, the HNCMs@Ni(OH)$_2$–6 electrode possessed the highest *C* value among these samples in account for the balance between adequate nickel hydroxide nanocrystals and reserved hierarchical nanoporous structure of HNCMs. Fig. 5**c** is the electrochemical impedance spectra (EIS) of the samples. Additionally, the equivalent circuit was used for quantitative analysis, and the detailed parameters were summarized in **Table S3**. Compared with other electrodes, the HNCMs@Ni(OH)$_2$–6 electrode exhibited the smallest charge transfer resistance (R_{ct}) and internal resistance (R_s), revealing its superior electrochemical conductivity and faster charge transfer process. (Yun et al., 2019; Wu et al., 2021). Furthermore, the slope in the low-frequency corresponds to the Warburg impedance (Ping et al., 2019b). Compared with the original Ni(OH)$_2$ electrode, the HNCMs@Ni(OH)$_2$ electrode showed a larger slope line, indicating that the introduction of HNCMs effectively improved the electrochemical conductivity and the diffusion rate of electrolyte ions.

Fig. 5**d** shows the CV curves of HNCMs@Ni(OH)$_2$–6 electrodes at various scan rates ranging from 5 to 100 mV/s. Obviously, the shape of the CV curves under different current densities do not significantly deform, whereas the current response increased with the increasing of scan rate, suggesting the good rate capability of the HNCMs@Ni(OH)$_2$–6 electrode (Feng et al., 2020; Lu et al., 2021b). Besides, all GCD curves obtained at various current densities also were similar with apparent potential plateaus (Fig. 5**e**). To make a comparison,

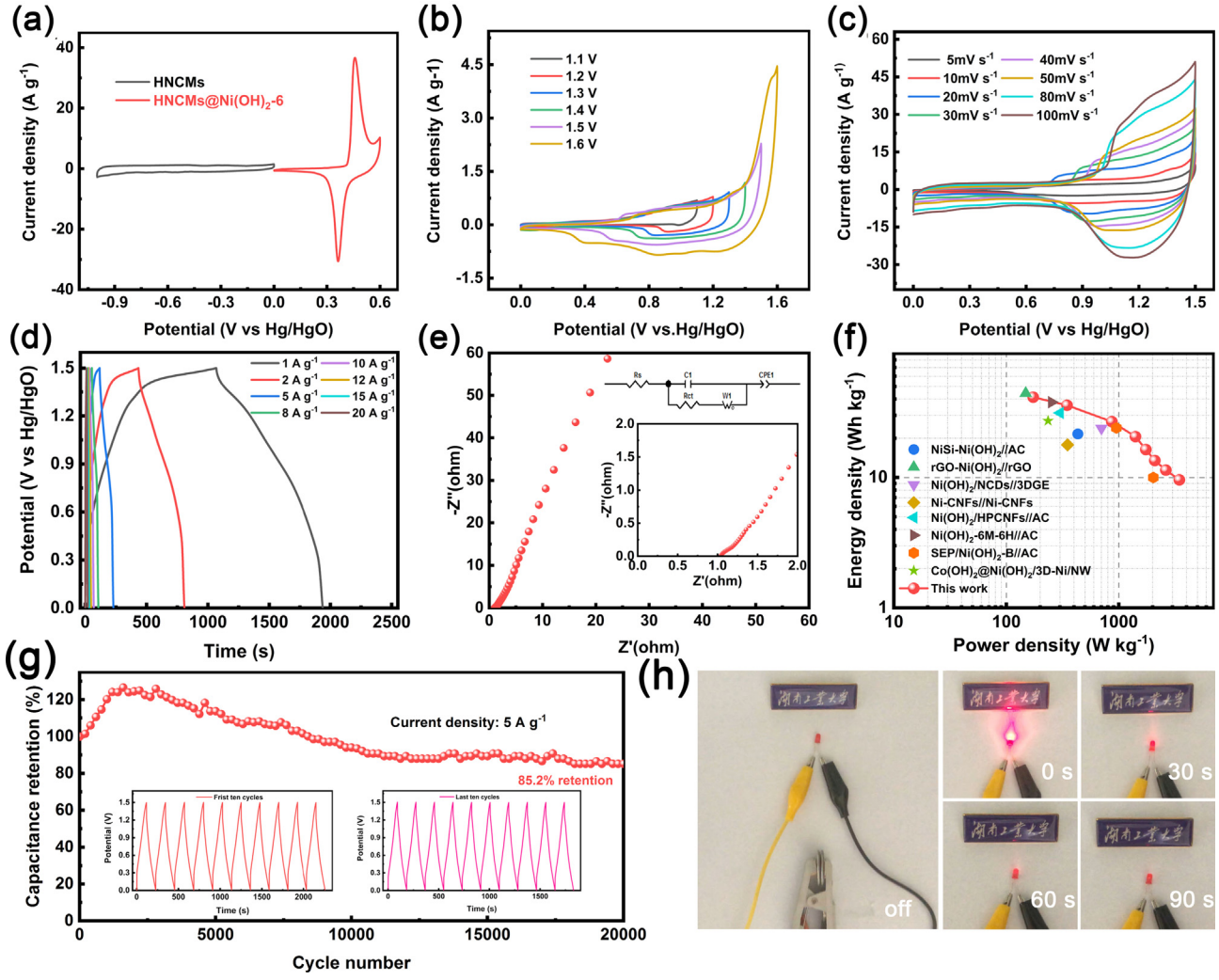

Fig. 6 (a) CV curves of the HNCMs electrode and HNCMs@Ni(OH)$_2$–6 electrode. (b) CV curves of the HNCMs@Ni(OH)$_2$–6//HNCMs in various potential windows. (c) CV curves of the HNCMs@Ni(OH)$_2$–6//HNCMs at different scan rates. (d) GCD curves of HNCMs@Ni(OH)$_2$–6//HNCMs at various current densities. (e) EIS curves of HNCMs@Ni(OH)$_2$–6//HNCMs. (f) Ragone plots of HNCMs@Ni(OH)$_2$–6//HNCMs. (g) Cycle property of HNCMs@Ni(OH)$_2$–6//HNCMs. (h) Photographs of lighted red LED by two connected hybrid supercapacitors (nominal voltage is 3 V).

the electrochemical properties of pure HNCMs and nickel hydroxide were also evaluated as shown in **Fig. S3a and b**. The *C* value of three electrodes including nickel hydroxide, HNCMs, and HNCMs@$Ni(OH)_2$–6 independence of current density were calculated and summarized in **Fig. S4**. Compared with nickel hydroxide electrode, HNCMs@$Ni(OH)_2$–6 electrode displayed higher value of *C* (248.9 mAh/g *vs* 125.7 mAh/g) and better rate performance (62.9% *vs* 51.9%). Besides, the HNCMs@$Ni(OH)_2$–6 electrode retained 81.1% of its initial capacity after 3000 cycles, while the nickel hydroxide electrode only had 50.0% capacity retention, indicating a great improvement in cycling performance. The HNCMs@$Ni(OH)_2$–6 electrode also showed competitive performance in comparison with the recently reported results of nickel hydroxide-based electrodes (**Table S4**). The synthesized HNCMs@$Ni(OH)_2$–6 in the application of capacitor exhibited superior cycling stability, enhanced specific capacity, and high rate performance attributed to the following aspects. Firstly, the introduction of HNCMs significantly improved the conductivity of $Ni(OH)_2$. Secondly, the interconnected hierarchically nanoporous structure of HNCMs in HNCMs@Ni$(OH)_2$–6 composite benefits the ion transportation inside the materials. Lastly, the unique structure of HNCMs@Ni$(OH)_2$–6 effectively avoided collapse and volume expansion of nickel hydroxide during the consecutive charging and discharging process.

3.3. Fabrication and electrochemical properties of HNCMs@Ni(OH)$_2$–6//HNCMs hybrid supercapacitor

A hybrid supercapacitor was assembled employing HNCMs@$Ni(OH)_2$–6 as cathode and HNCMs as anode, and the mass ratio of HNCMs@$Ni(OH)_2$–6 to HNCMs in the two electrodes was set to be 0.3:1 according to **Eq. (2)**. Based on curves scanned at 5 mV/s in Fig. 6**a,** the potential window of −1–0 V for HNCMs and the potential window of 0–0.6 V of HNCMs@$Ni(OH)_2$–6 suggested that the operating potential window of the hybrid supercapacitor was in the range of 0–1.6 V. Subsequently, a series of CV curves of the hybrid supercapacitor was recorded with the operating voltage changing from 1.1 V to 1.6 V at 5 mV/s (Fig. 6**b**). Obviously, the CV curve obtained at 1.6 V was significantly deformed due to the polarization phenomenon. Thus, the optimal potential window in the range of 0–1.5 V was eventually applied. Fig. 6**c** displayed the CV curves of the hybrid supercapacitor scanned from 5 to 100 mV/s. As shown, the curves were well retained in shape without obvious deformation even at 100 mV/s of high scan rate. Moreover, all GCD curves scanned from 1 to 20 A/g (Fig. 6**d**) were nearly symmetrical, indicative of the excellent electrochemical reversibility and high coulomb efficiency of the hybrid supercapacitor (Gao et al., 2020). According to discharge time and **Eq. (3)**, the calculated specific capacitances (C_H) were 132.1, 114.4, 85.6, 65.8, 52.4, 43.3, 36.6, and 30.8F/g at 1, 2, 5, 8, 10, 12, 15, and 20 A/g, respectively. The electrochemical impedance spectrum in Fig. 6**e** showed the R_s and the R_{ct} of hybrid supercapacitor were 1.26 Ω and 0.37 Ω, respectively, revealing the good electrochemical conductivity (Yang et al., 2021; Li et al., 2019). In general, the value of *E* and *P* have been considered to be two critical indicators for evaluating the commercial application value of hybrid supercapacitors. Fig. 6**f** showed that the hybrid supercapacitor delivered a maximum *E* value of 41.3 Wh/kg at a *P* value of 173.3 W/kg, and still maintained a decent *E* value of 9.6 Wh/kg even at a high *P* value of 3.4 kW/kg. These properties were comparable or even higher than reported $Ni(OH)_2$-based hybrid supercapacitors (**Table S5**). Finally, the cycling property of the assembled hybrid supercapacitor was estimated at 5 A/g (Fig. 6**g**). The results showed that the value of *C* increased in the first 3000 cycles, which might be owing to the gradual activation of the electrode, leading to a larger electroactive surface area and more channels for the transportation of electrons and ions (Zhang et al., 2020; Wu et al., 2019, Lokhande et al., 2020c). After 20,000 cycles, 85.2% capacity retention was maintained. Besides, the inset in Fig. 6**g** showed the similar shape of the first/last ten cycles, suggesting superior electrochemical reversibility and cycling stability. As a proof of concept example, two connected charged hybrid supercapacitors can successfully illuminate a red LED (nominal voltage is 3 V) (Fig. 6**h**), demonstrating the potential application value of the hybrid supercapacitor.

4. Conclusions

In conclusion, well-defined core–shell structured rambutan-like HNCMs@$Ni(OH)_2$ microspheres were prepared by facile in-situ chemical deposition of nickel hydroxide nanocrystals on HNCMs. It is found that the Ni^{2+} concentration in the system could effectively regulate the surface structure and electrochemical properties of the resultant HNCMs@$Ni(OH)_2$ electrodes. By keeping the concentration of Ni^{2+} in solution at 0.12 M, HNCMs@$Ni(OH)_2$–6 rambutan-like microspheres with suitable deposition amount of nickel hydroxide nanocrystals and well-retained hierarchical nanoporous structure can be prepared. Ascribed to the high *C* value of nickel hydroxide and the interconnected hierarchical porous structure of HNCMs, the resultant rambutan-like HNCMs@$Ni(OH)_2$ microspheres display outstanding electrochemical properties including a high *C* value (248.9 mAh/g at 1 A/g) and splendid rate performance (the capacitance retention of 62.9% at 20 A/g) as electrode materials. Furthermore, a hybrid supercapacitor with rambutan-like HNCMs@$Ni(OH)_2$ microspheres as cathode and HNCMs as anode were assembled, which showed a comparable *E* value of 41.3 Wh/kg at a *P* value of 173.3 W/kg and good cycling stability with 85.2% initial capacity retention through 20,000 cycles at 5 A/g. It is anticipated that as-prepared HNCMs@$Ni(OH)_2$ microspheres will have great application prospects in the fabrication of advanced energy storage devices.

Declaration of Competing Interest

The authors declare that they have no known competing financial interests or personal relationships that could have appeared to influence the work reported in this paper.

Acknowledgments

The financial support by the National Natural Science Foundation of China (52174247, 51974116 and 51874128), the Natural Science Foundation of Hunan Province (2021JJ30211, 2020JJ4273 and 2020JJ5130), the Scientific Research Fund of Hunan Provincial Education Department (19B158) is gratefully acknowledged.

Appendix A. Supplementary material

Supplementary data to this article can be found online at https://doi.org/10.1016/j.arabjc.2021.103580.

References

Afif, A., Rahman, S.M., Azad, A.T., Zaini, J., Islan, M.A., Azad, A. K., 2019. Advanced materials and technologies for hybrid supercapacitors for energy storage – A review. J. Energy Storage 25, 100852.

Abitkar, S.B., Jadhav, P.R., Tarwal, N.L., Moholkar, A.V., Patil, C. E., 2019. A facile synthesis of α-$Ni(OH)_2$-CNT composite films for supercapacitor application. Adv. Powder Technol. 30, 2285–2292.

Brisse, A.-L., Stevens, P., Toussaint, G., Crosnier, O., Brousse, T., 2018. $Ni(OH)_2$ and NiO based composites: battery type electrode materials for hybrid supercapacitor devices. Materials 11, 1178.

Choi, C., Ashby, D.S., Butts, D.M., DeBlock, R.H., Wei, Q.L., Lau, J., Dunn, B., 2020. Achieving high energy density and high power density with pseudocapacitive materials. Nat. Rev. Mater. 5, 5–19.

Che, H.W., Lv, Y.M., Liu, A.F., Li, H.G., Guo, Z.C., Mu, J.B., Wang, Y.M., Zhang, X.L., 2020. $MnCo_2O_4$@$Co(OH)_2$ coupled with N-doped carbon nanotubes@reduced graphene oxide nanosheets as electrodes for solid-state asymmetric supercapacitors. Chem. Eng. J. 384, 123372.

Chodankar, N.R., Pham, H.D., Nanjundan, A.K., Fernando, J.F.S., Jayaramulu, K., Golberg, D., Han, Y.-K., Dubal, D.P., 2020. True meaning of pseudocapacitors and their performance metrics: Asymmetric versus hybrid supercapacitors. Small 16, 2002086.

Chen, K., Liu, J.X., Bian, H.L., Wei, J., Wang, W.J., Shao, Z.Q., 2020. Ingenious preparation of N/NiO_x co-doped hierarchical porous carbon nanosheets derived from chitosan nanofibers for high performance supercapacitors. Nanotechnology 31, 335713.

Chavan, U.S., Lokhande, P.E., Bhosale, S., 2021. Nickel hydroxide nanosheets grown on nickel foam for high performance supercapacitor applications. Mater. Technol. https://doi.org/10.1080/10667857.2021.1873636.

Du, Y.Q., Xiao, P., Yuan, J., Chen, J.W., 2020. Research Progress of Graphene-Based Materials on Flexible Supercapacitors. Coat. 10, 892.

Choi, J., Kim, M., Kim, J., 2017. Correlation between the mesoporous carbon sphere with $Ni(OH)_2$ nanoparticle contents for high-performance supercapacitor electrode. Ionics 24, 815–825.

Du, Y.T., Mo, Y., Chen, Y., 2021. Effects of Fe Impurities on Self-Discharge Performance of Carbon-Based Supercapacitors. Mater. 14, 1908.

Fu, Y.S., Zhou, Y., Peng, Q., Yu, C.Y., Wu, Z., Sun, J.W., Zhu, J.W., Wang, X., 2018. Hollow mesoporous carbon spheres enwrapped by small-sized and ultrathin nickel hydroxide nanosheets for high-performance hybrid supercapacitors. J. Power Sources 402, 43–52.

Feng, X., Ning, J., Wang, D., Zhang, J.C., Xia, M.Y., Wang, Y., Hao, Y., 2020. Heterostructure arrays of $NiMoO_4$ nanoflakes on N-doping of graphene for high-performance asymmetric supercapacitors. J. Alloys Compd. 816, 152625.

Gonçalves, J.M., Silva, M.I., Toma, H.E., Angnes, L., Martins, P.R., Araki, K., 2020. Trimetallic oxides/hydroxides as hybrid supercapacitors electrode materials: A review. J. Mater. Chem. A 8, 10534–10570.

Gao, X.Y., Zhao, Y.F., Dai, K.Q., Wang, J.T., Zhang, B., Shen, X.J., 2020. NiCoP nanowire@NiCo-layered double hydroxides nanosheet heterostructure for flexible asymmetric supercapacitors. Chem. Eng. J. 384, 123372.

Guo, Q.F., Yuan, J.Z., Tang, Y.B., Song, C.X., Wang, D.B., 2021. Self-assembled PANI/CeO_2/$Ni(OH)_2$ hierarchical hybrid spheres with improved energy storage capacity for high-performance supercapacitors. Electrochim. Acta 367, 137525.

Han, J.Z., Ping, Y.J., Li, J.J., Liu, Z., Xiong, B.Y., Fang, P.F., He, C. Q., 2019. One-step nitrogen, boron codoping of porous carbons derived from pomelo peels for supercapacitor electrode materials. Diamond Relat. Mater. 96, 176–181.

Han, J.Z., Ping, Y.J., Yang, S.J., Zhang, Y.M., Qian, L.B., Li, J.J., Liu, L., Xiong, B.Y., Fang, P.F., He, C.Q., 2020. High specific power/energy, ultralong life supercapacitors enabled by cross-cutting bamboo-derived porous carbons. Diamond Relat. Mater. 109, 108044.

Hong, Y.W., Yang, J.X., Choi, W.M., Wang, J.J., Xu, J.L., 2021a. B-doped g-C_3N_4 quantum dots-modified $Ni(OH)_2$ nanoflowers as an efficient and stable electrode for supercapacitors. ACS Appl. Energy Mater. 4, 1496–1504.

Hong, X.D., Fu, J.W., Liu, Y., Li, S.L., Liang, B., 2021b. Strawberry-like carbonized cotton Cloth@Polyaniline nanocomposite for high-performance symmetric supercapacitors. Mater. Chem. Phys. 258, 123999.

Jiang, J.B., Chen, Y.K., Hu, X.M., Cong, H.S., Zhou, Q.Y., Rong, H. B., Sun, Y.X., Han, S., 2020. Designed synthesis of 2D multilayer $CuCo_2S_4$ nanomaterials for high-performance asymmetric supercapacitors. Vac. 182, 109698.

Jing, L.L., Zhang, L., Li, G.H., Guo, Z.R., Li, Z.H., Li, Z.J., Yao, H. C., Wang, J.S., Liu, Q.C., 2021. Rapid and large-scale synthesis of polydopamine based N-doped carbon spheres@$Co_xNi_{1-x}(OH)_2$ core-shell nanocomposites for high performance supercapacitors. J. Alloys Compd. 854, 157246.

Ji, Z.Y., Ma, D.W., Dai, W.Y., Liu, K., Shen, X.P., Zhu, G.X., Nie, Y. J., Pasang, D., Yuan, A.H., 2021. Anchoring nitrogen-doped carbon quantum dots on nickel carbonate hydroxide nanosheets for hybrid supercapacitor applications. J. Colloid Interf. Sci. 590, 614–621.

Liu, F.Y., Chu, X., Zhang, H.T., Zhang, B.B., Su, H., Jin, L., Wang, Z.X., Huang, H.C., Yang, W.Q., 2018. Synthesis of self-assembly 3D porous $Ni(OH)_2$ with high capacitance for hybrid supercapacitors. Electrochim. Acta 269, 102–110.

Lokhande, P.E., Chavan, U.S., 2018. Nanoflower-like $Ni(OH)_2$ synthesis with chemical bath deposition method for high performance electrochemical applications. Mater. Lett. 218, 225–228.

Liu, Y.K., Jiang, G.H., Huang, Z., Lu, Q.L., Yu, B., Evariste, U., Ma, P., 2019. Decoration of hollow mesoporous carbon spheres by $NiCo_2S_4$ nanoparticles as electrode materials for asymmetric supercapacitors. ACS Appl. Energy Mater. 2, 8079–8089.

Lokhande, P.E., Chavan, U.S., 2019. Nanostructured $Ni(OH)_2$/rGO composite chemically deposited on Ni foam for high performance of supercapacitor applications. Mater. Sci. Energy Technol. 2, 52–56.

Li, J.Y., Yun, X.R., Hu, Z.L., Xi, L.J., Li, N., Tang, T., Lu, P.C., Zhu, Y.R., 2019. Three-dimensional nitrogen and phosphorus co-doped carbon quantum dots/reduced graphene oxide composite aerogels with hierarchical porous structure as superior electrode materials for supercapacitors. J. Mater. Chem. A 7, 26311–26325.

Liu, H., Liu, X., Wang, S.L., Liu, H.K., Li, L., 2020. Transition metal based battery-type electrodes in hybrid supercapacitors: A review. Energy Storage Mater. 28, 122–145.

Li, J.B., Liu, Y., Cao, W., Chen, N., 2020. Rapid in situ growth of β-$Ni(OH)_2$ nanosheet arrays on nickel foam as an integrated electrode for supercapacitors exhibiting high energy density. Dalton Trans. 49, 4956–4966.

Lokhande, P.E., Chavan, U.S., Pandey, A., 2020a. Materials and fabrication methods for electrochemical supercapacitors: overview. Electrochem. Energ. Rev. 3, 155–186.

Lokhande, P.E., Chavan, U.S., 2020b. Cyclic voltammetry behavior modeling of fabricated nanostructured $Ni(OH)_2$ electrode using artificial neural network for supercapacitor application. J Mechanical Engineering Science 234, 2563–2568.

Lokhande, P.E., Chavan, U.S., 2020c. All-Solid-State asymmetric supercapacitor based on Ni–Co layered double hydroxide and rGO

nanocomposite deposited on Ni foam. J. Electrochem. En. Conv. Stor. 17, 1–14.
Lu, Y., Liu, Y.B., Mo, J.M., Deng, B.L., Wang, J.X., Zhu, Y.Q., Xiao, X.D., Xu, G., 2021a. Construction of hierarchical structure of Co_3O_4 electrode based on electrospinning technique for supercapacitor. J. Alloys Compd. 853, 157271.
Lu, Y., Deng, B.L., Liu, Y.B., Wang, J.X., Tu, Z.K., Lu, J.M., Xiao, X.D., Xu, G., 2021b. Nanostructured Co_3O_4 for achieving high-performance supercapacitor. Mater. Lett. 285, 129101.
Liang, R.B., Du, Y.Q., Xiao, P., Cheng, J.Y., Yuan, S.J., Chen, Y.L., Yuan, J., Chen, J.W., 2021. Transition metal oxide electrode materials for supercapacitors: A review of recent developments. Mater. Sci. Nanomaterials 11, 1248.
Luo, X.Y., Chen, Y., Mo, Y., 2021. A review of charge storage in porous carbon-based supercapacitors. New Carbon Mater. 36, 49–65.
Muzaffar, A., Ahamed, M.B., Deshmukh, K., Thirumalai, J., 2019. A review on recent advances in hybrid supercapacitors: Design, fabrication and applications. Renew. Sust. Energ. Rev. 101, 123–145.
Mohammed, M.M.M., Abd-Elrahim, A.G., Chun, D.-M., 2020. One-step deposition of a $Ni(OH)_2$-graphene hybrid prepared by vacuum kinetic spray for high energy density hybrid supercapacitor. Mater. Chem. Phys. 244, 122701.
Nguyen, T., Montemor, M.F., 2019. Metal oxide and hydroxide–based aqueous supercapacitors: from charge storage mechanisms and functional electrode engineering to need-tailored devices. Adv. Sci. 6, 1801797.
Ou, P., Zhou, Q.Y., Li, J., Chen, W., Huang, J.G., Yang, L.Q., Liao, J., Sheng, M.Q., 2019. Facile ethylene glycol-assisted hydrothermal synthesis of MoO_2 nanospheres for high-performance supercapacitors. Mater. Res. Express 6, 095044.
Ping, Y.J., Liu, Z., Li, J.J., Han, J.Z., Yang, Y.P., Xiong, B.Y., Fang, P.F., He, C.Q., 2019a. Boosting the performance of supercapacitors based hierarchically porous carbon from natural Juncus effuses by incorporation of MnO_2. J. Alloys Compd. 805, 822–830.
Ping, Y.J., Han, J.Z., Li, J.J., Xiong, B.Y., Fang, P.F., He, C.Q., 2019b. N, S co-doped porous carbons from natural Juncus effuses for high performance supercapacitors. Diamond Relat. Mater. 100, 107577.
Raza, W., Ali, F., Raza, N., Luo, Y.W., Kim, K.-H., Yang, J.H., Kumar, S., Mehmood, A., Kwon, E.E., 2018. Recent advancements in supercapacitor technology. Nano Energy 52, 441–473.
Simon, P., Gogotsi, Y., Dunn, B., 2014. Where do batteries end and supercapacitors begin? Mater. Sci. 343, 1210–1211.
Shakir, I., Almutairi, Z.A., Shar, S.S., Nafady, A., 2020. Nickel hydroxide nanoparticles and their hybrids with carbon nanotubes for electrochemical energy storage applications. Results Phys. 17, 103117.
Tang, H., Yao, J.J., Zhu, Y.R., 2021. Recent developments and future prospects for Zinc-Ion hybrid capacitors: A review. Adv. Energy Mater. 11, 2003994.
Wang, Y., Wang, Y.C., Jiang, L., 2018. Freestanding carbon aerogels produced from bacterial cellulose and its $Ni/MnO_2/Ni(OH)_2$ decoration for supercapacitor electrodes. J. Appl. Electrochem. 48, 495–507.
Wang, Q.S., Zhang, Y.F., Xiao, J.Q., Jiang, H.M., Li, X.J., Meng, C. G., 2019. Novel ordered hollow spherical nickel silicate-nickel hydroxide united composite with two types of morphologies for enhanced electrochemical storage performance. Mater. Chem. Front. 3, 2090–2101.
Wu, C., Zhu, Y., Guan, C., Jia, C.K., Qin, W., Wang, X.Y., Zhang, K. L., 2019. Mesoporous aluminium manganese cobalt oxide with pentahedron structures for energy storage devices. J. Mater. Chem. A 7, 18417–18427.
Upadhyay, K.K., Bundaleska, N., Abrashev, M., Bundaleski, N., Teodoro, O.M.N.D., Fonseca, I., Ferro, A.M., Silva, R.P., Tatarova, E., Montemor, M.F., 2019. Free-standing N-graphene as conductive matrix For $Ni(OH)_2$ based supercapacitive electrodes. Electrochim. Acta 334, 135592.
Wang, H., Shao, Y., Mei, S.L., Lu, Y., Zhang, M., Sun, J.-K., Matyjaszewski, K., Antonietti, M., Yuan, J.Y., 2020. Polymer-derived heteroatom-doped porous carbon materials. Chem. Rev. 120, 9363–9419.
Wu, X.H., Chen, Y.H., Lian, K.J., Yu, X.A., Zhuang, Q.Q., Yang, Q., Liu, S.F., Liao, S., Li, N., Zhang, H., 2021. Fe_2O_3 nanowire arrays on Ni-coated yarns as excellent electrodes for high performance wearable yarn-supercapacitor. J. Alloys Compd. 866, 158156.
Xu, M., Yu, Q., Liu, Z.H., Lv, J.S., Lian, S.T., Hu, B., Mai, L.Q., Zhou, L., 2018. Tailoring porous carbon spheres for supercapacitors. Nanoscale 10, 21604.
Xu, J.X., Du, G., Xie, L., Yuan, K., Zhu, Y.R., Xu, L.J., Li, N., Wang, X.Y., 2020. Three-dimensional walnut-like, hierarchically nanoporous carbon microspheres: One-pot synthesis, activation, and supercapacitive performance. ACS Sustainable Chem. Eng. 8, 8024–8036.
Xie, L., Yuan, K., Xu, J.X., Zhu, Y.R., Xu, L.J., Li, N., Du, J.J., 2020. Comparative study on supercapacitive performances of hierarchically nanoporous carbon materials with morphologies from submicrosphere to hexagonal microprism. Front. Chem. 8, 599981.
Yan, J., Wang, Q., Wei, T., Fan, Z.J., 2014. Recent advances in design and fabrication of electrochemical supercapacitors with high energy densities. Adv. Energy Mater. 4, 1300816.
Yang, S.J., Ping, Y.J., Qian, L.B., Han, J.Z., Xiong, B.Y., Li, J.J., Fang, P.F., He, C.Q., 2019a. Flower-like Bi_2O_3 with enhanced rate capability and cycling stability for supercapacitors. J. Mater. Sci. Mater. Electron. 31, 2221–2230.
Yao, M.Y., Zhao, X., Zhang, J.X., Tan, W.J., Luo, J., Dong, J., Zhang, Q.H., 2019. Flexible all-solid-state supercapacitors of polyaniline nanowire arrays deposited on electrospun carbon nanofibers decorated with MOFs. Nanotechnol. 30, 085404.
Yang, X.X., Fu, K., Mao, L.C., Peng, W., Jin, J.H., Yang, S.L., Li, G., 2019b. Bio-mediated synthesis of α-$Ni(OH)_2$ nanobristles on hollow porous carbon nanofibers for rechargeable alkaline batteries. Chem. Eng. Sci. 205, 269–277.
Yun, X.R., Li, J.Y., Chen, X.H., Chen, H., Xiao, L., Xiang, K.X., Chen, W.H., Liao, H.Y., Zhu, Y.R., 2019. Porous Fe_2O_3 modified by nitrogen-doped carbon quantum dots/reduced graphene oxide composite aerogel as a high-capacity and high-rate anode material for alkaline aqueous batteries. ACS Appl. Mater. Inter. 11, 36970–36984.
Yang, S.J., Qian, L.B., Ping, Y.J., Zhang, H.L., Li, J.J., Xiong, B.Y., Fang, P.F., He, C.Q., 2021. Electrochemical performance of Bi_2O_3 supercapacitors improved by surface vacancy defects. Ceram. Int. 47, 8290–8299.
Zhang, L.Y., Shi, D.W., Liu, T., Jaroniec, M., Yu, J.G., 2018a. Nickel-based materials for supercapacitors. Mater. Today 25, 35–65.
Zhou, Q.Y., Fan, T.W., Li, Y.Y., Chen, D.C., Liu, S.L., Li, X., 2019. Hollow-structure NiCo hydroxide/carbon nanotube composite for high-performance supercapacitors. J. Power Sources 624, 111–115.
Zeng, L., Lou, X.C., Zhang, J.H., Wu, C., Liu, J., Jia, C.K., 2019. Carbonaceous mudstone and lignin-derived activated carbon and its application for supercapacitor electrode. Surf. Coat. Technol. 357, 580–586.
Zhang, Y.F., Fan, W., Lu, H.Y., Liu, T.X., 2018b. Highly porous polyimide-derived carbon aerogel as advanced three-dimensional framework of electrode materials for high-performance supercapacitors. Electrochim. Acta 283, 1763–1772.
Zhang, S., Wu, C.L., Wu, W., Zhou, C., Xi, Z.W., Deng, Y.Y., Wang, X., Quan, P.P., Li, X.J., Luo, Y.F., 2019. High performance flexible supercapacitors based on porous wood carbon slices derived from Chinese fir wood scraps. J. Power Sources 424, 1–7.
Zhou, S.Y., Liu, Y., Yan, M., Sun, L., Luo, B.F., Yang, Q.J., Shi, W. D., 2020a. Design of $FeCo_2S_4$@$Ni(OH)_2$ core-shell hollow nanotube arrays on carbon paper for ultra-high capacitance in supercapacitors. Electrochim. Acta 349, 136337.

Zhou, Y.T., Liu, M., Yang, H.Y., Liu, Q., Li, W.D., Yu, C.-M., 2020b. Porous graphene oxide nanosheets warped by $Ni(OH)_2$ platelets as an efficient binder-free electrode material for supercapacitors. Synth. Met. 267, 116452.

Zhang, L., Li, G.H., Jing, L.L., Li, Z.H., Li, Z.J., Yao, H.C., Wang, J.S., Liu, Q.C., Han, Y., 2020. Controllable and fast growth of ultrathin α-$Ni(OH)_2$ nanosheets on polydopamine based N-doped carbon spheres for supercapacitors application. Synth. Met. 270, 116580.